Thermoluminescence and EPR studies of nanocrystalline Nd_2O_3:Ni^{2+} phosphor

B. Umesh [a,b], B. Eraiah [b], H. Nagabhushana [c,*], S.C. Sharma [c], D.V. Sunitha [c], B.M. Nagabhushana [d], C. Shivakumara [e], J.L. Rao [f], R.P.S. Chakradhar [g,**]

[a] Department of Humanities, PVP Polytechnic, Dr. AIT Campus, Bangalore 560056, India
[b] Department of Physics, Bangalore University, Bangalore 560056, India
[c] Prof C.N.R. Rao Centre for Nano Research (CNR), Tumkur University, Tumkur 572103, India
[d] Department of Chemistry, M.S. Ramaiah Institute of Technology, Bangalore 560054, India
[e] Solid State and Structural Chemistry Unit, Indian Institute of Science, Bangalore 560012, India
[f] Department of Physics, S.V. Univeristy, Tirupathi 517502, India
[g] National Aerospace Laboratories (CSIR), Bangalore 560017, India

ARTICLE INFO

ABSTRACT

Nanocrystalline Nd_2O_3:Ni^{2+} (2 mol%) phosphor has been prepared by a low temperature ($\sim$400 °C) solution combustion method, in a very short time (<5 min). Powder X-ray diffraction results confirm the single hexagonal phase of nanopowders. Scanning electron micrographs show that nanophosphor has porous nature and the particles are agglomerated. Transmission electron microscopy confirms the nanosize (20–25 nm) of the crystallites. The electron paramagnetic resonance (EPR) spectrum exhibits a symmetric absorption at $g \approx 2.77$ which suggests that the site symmetry around Ni^{2+} ions is predominantly octahedral. The number of spins participating in resonance (N) and the paramagnetic susceptibility (χ) has been evaluated. Raman study show major peaks, which are assigned to F_g and combination of $A_g + E_g$ modes. Thermoluminescence (TL) studies reveal well resolved glow peaks at 169 °C along with shoulder peak at around 236 °C. The activation energy (E in eV), order of kinetics (b) and frequency factor (s) were estimated using glow peak shape method. It is observed that the glow peak intensity at169 °C increases linearly with γ-dose which suggest that Nd_2O_3:Ni^{2+} is suitable for radiation dosimetry applications.

© 2012 Elsevier B.V. All rights reserved.

1. Introduction

Rare earth oxides have been widely used as high-performance luminescent devices, magnets, and other functional materials based on the electronic, optical, and chemical characteristics arising from their 4f electrons [1,2]. Most of these advanced functions depend strongly on the compositions and structures, which are sensitive to the bonding states of rare earth atoms or ions. If rare earth oxides are fabricated in the form of a nanostructure, they will hold potential as highly functionalized materials as a result of both shape-specific and quantum confinement effects. They could also act as electrically, magnetically, or optically functional host materials [3]. Among rare earth oxides, Neodymium oxide (Nd_2O_3) is widely used in photonic applications (as phosphors providing yellow-to-violet upconversion emission) [4], as components for advanced materials (high temperature ceramics and superconductors) [5,6], as components of catalytic systems (oxidative coupling of methane, N_2 decomposition, dehydrogenation of alcohols,

high-temperature processes) [7]. In thin film form it has highly useful as optical anti reflection coatings, gate insulators and protective coatings. For most of these applications the ultrafine (in nanometric scale) neodymium oxide with well-defined particle morphology is the most interesting material.

Solution-based chemical synthesis such as hydrothermal, sol–gel, chemical co-precipitation and combustion have received considerable attention since they offer the possibilities for controlling homogeneity, purity of phase, size distribution, surface area and microstructural uniformity of the phosphors. However, co-precipitation processes involve repeated washing to eliminate the anions coming from the precursor salts used, making the process complicated and very time-consuming. Solution combustion synthesis is another wet-chemical method, which has been proved to be an excellent technique for preparing several grams of micro/nanocrystalline phosphors due to its short processing time, low processing temperature, low cost, and high yield, as well as good ability to achieve high purity in making single or multi phase complex oxide powders at the as-synthesized state [8,9]. In comparison with other methods, the products obtained by the combustion synthesis method are generally more homogeneous, have less impurity, and have higher surface areas than powders prepared by conventional methods [10,11].

* Corresponding author. Tel.: +91 9945954010 (M).
** Corresponding author.
 E-mail address: bhushanvlc@gmail.com (H. Nagabhushana).

As a part of our programme on nanomaterials, here we report the preparation of Nd_2O_3:Ni^{2+} nano phosphor by a low temperature solution combustion method. The synthesized powders are well characterized by using Powder X-ray diffraction (PXRD), scanning electron microscopy (SEM), and transmission electron microscopy (TEM), UV–vis, Raman and electron paramagnetic resonance (EPR) spectroscopy. In addition, thermoluminescent (TL) properties were also investigated. It is known that the TL process in phosphors is in generally related to the defect centers created due to ionizing radiation. TL investigations have also shown that defect centers play a crucial role in TL. The formation and the stability of the defect centers also depend on the method of preparation of phosphors and dopants. Therefore, the objective of the present work is to investigate the TL properties of Nd_2O_3:Ni^{2+} nanopowder concerning to its structural, morphological, and luminescent characteristics and to propose it as a good candidate TL dosimeter for gamma radiation field.

2. Experimental

2.1. Synthesis of Nd_2O_3:Ni nano phosphor

For the preparation of Nd_2O_3:Ni^{2+} (2 mol%) phosphor, the starting chemicals used in the present study were of analar grade neodymium nitrate ($Nd(NO_3)_3$), nickel nitrate ($Ni(NO_3)_3$) and oxalyl dihydrazide ($C_2H_6N_4O_2$; ODH). The stoichiometric amounts were dissolved in a minimum quantity of doubled distilled water in a cylindrical Petri dish of approximate 150 ml capacity. ODH was used as a fuel in the combustion synthesis and it is prepared in our laboratory by the reaction of diethyl oxalate and hydrazine hydrate as described in the literature [12]. The mixture was dispersed well using a magnetic stirrer for about 5 min. A Petri dish containing the heterogeneous mixture was placed in a pre-heated muffle furnace maintained at $400 \pm 10\,^{\circ}C$. The reaction mixture initially undergoes thermal dehydration followed by ignition with liberation of large gaseous products such as oxides of nitrogen and carbon. Finally, a voluminous and foamy greenish product has been obtained. The product of the combustion reaction was then given an annealing treatment at $900\,^{\circ}C$ for 3 h in air to remove the thermal stress and impurities during its preparation. After being annealed, the brown–black powder became white and this was used for further characterization.

The powder X-ray diffraction studies have been carried out using by using an X-ray diffractometer PANalytical X'pert Pro, Almelo, (The Netherlands) with Cu Kα radiation ($\lambda = 1.5405\,\text{Å}$). The average crystallite size (d) was calculated from the diffraction line width of X-rays. The crystallite size was estimated from the broad PXRD peaks using the Scherer's equation $d = 0.9\lambda/\beta\cos\theta$ [13] where d is the average grain size of the crystallites, λ the incident wavelength, θ the Bragg angle and β the diffracted full-width at half-maximum (FWHM) in radians caused by the crystallites. The strain effect can be estimated by W–H plots using the equation [14] $\beta\cos\theta = \varepsilon(4\sin\theta) + \lambda/D$ where β (FWHM in radian) is measured for different XRD lines corresponding to different planes, ε is the strain developed and D is the grain size. The equation represents a straight line between $4\sin\theta$ (X-axis) and $B\cos\theta$ (Y-axis). The slope of line gives the strain (ε) and intercept (λ/D) of this line on the Y-axis gives grain size (D). The surface morphology of the samples has been examined using scanning electron microscopy (JEOL JSM 840A). TEM analysis was performed on a Hitachi H-8100 (accelerating voltage up to 200 kV, LaB_6 filament) equipped with EDS (Kevex Sigma TM Quasar, USA). The UV–vis spectra were recorded on a UV-3101 Shimadzu Visible spectrophotometer. Raman spectroscopic studies were performed on Renishaw In-via Raman spectrometer with 633 nm He–Cd laser and a Leica DMLM optical microscope
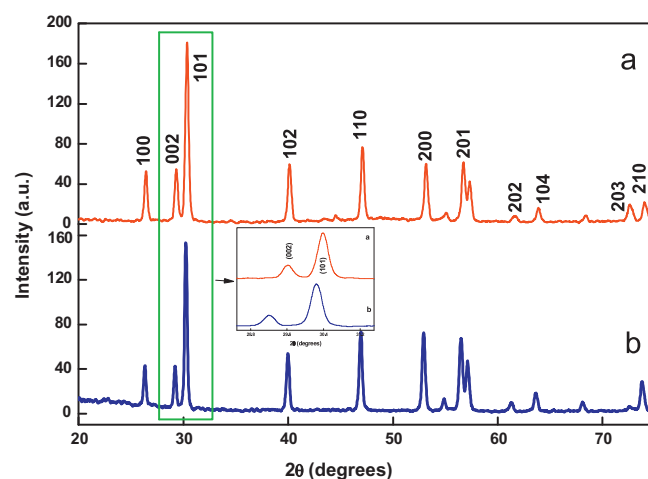

Fig. 1. PXRD patterns of un-doped and Ni^{2+} doped Nd_2O_3 nanophosphor.

equipped with $50\times$ objective, thus providing a laser spot of 2 μm in diameter. The EPR spectra were recorded at room temperature on a JEOL-FE-1X EPR spectrometer operating in the X-band (about 9.205 GHz) with a field modulation frequency of 100 kHz. The magnetic field was scanned from 0 to 500 mT and the microwave power used was 5 mW. A powdered glass specimen of 100 mg was taken in a quartz tube for EPR measurements. TL measurements were carried out at room temperature using Nucleonix TL reader using (^{60}C) gamma source as excitation in the dose range 0.228–2.057 kGy.

3. Results and discussion

3.1. Powder X-ray diffraction (PXRD)

Fig. 1 shows the PXRD patterns of un-doped and Ni doped Nd_2O_3 phosphor. The 2θ peaks at $\sim 29.7^{\circ}$, 47.0° and 53.0° correspond to hexagonal phase with A-type of Nd_2O_3 (JCPDS No. 24-0779). No additional peaks corresponding to any secondary or impurity phase were observed which confirms the phase purity of the sample. The average particle size of un-doped and Ni doped Nd_2O_3 was estimated using Scherer's equation [13] and is found to be in the range 21–28 nm. It is observed that a small shift in the position of main peaks to the lower side of 2θ values and broadening of XRD peaks are observed for Ni^{2+} doped sample. A peak shift in XRD profiles arises due to either presence of micro strains or purely size effect [15]. The W–H plots of un-doped and Ni^{2+} doped Nd_2O_3 phosphor is shown in (Fig. S1). The grain size determined from W–H formula is slightly higher than those calculated using Scherrer's formula. The small variation in the values is due to the fact that in Scherrer's formula strain component is assumed to be zero and observed broadening of diffraction peak is considered as a result of reducing grain size only. Further, it is observed that the strain for Ni^{2+} doped sample (6.4×10^{-3}) is greater than that of un-doped Nd_2O_3 (2.0×10^{-3}). This increase in strain causes the broadening and shift in XRD peaks in Ni^{2+} doped sample (inset of Fig. 1). The estimated values of crystallite size and strain for undoped and Ni^{2+} doped Nd_2O_3 from Scherer's equation and W–H plots are given in Table 1.

Table 1
Crystallite size, band gap and strain of un-doped and Ni^{2+} doped Nd_2O_3 nanophosphor.

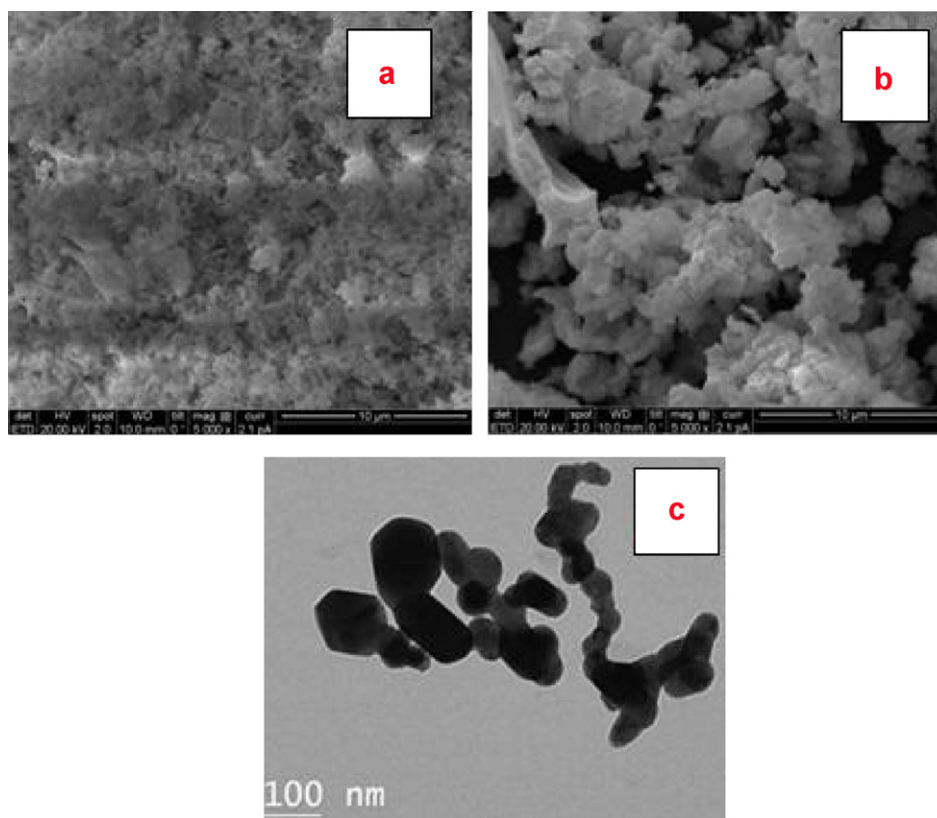| Nd_2O_3	Scherer's formula (nm)	W–H method (nm)	Strain (10^{-3})	Band gap (eV)
Un-doped	21	22	2.0	4.43
Ni doped	28	33	6.4	5.30

Fig. 2. SEM images of (a) un-doped Nd_2O_3 (b) Ni^{2+} doped Nd_2O_3; (c) TEM image of Ni^{2+} doped Nd_2O_3 nano phosphor.

3.2. Scanning and transmission electron microscopy (SEM and TEM)

Fig. 2(a and b) shows scanning electron micrographs of the undoped and doped samples. Undoped sample showing weekly agglomerated lumps composed of uniform size particles with pores and cracks. The mean particle size of powder is ranging from 50 to 120 nm. The doped Fig. 2(b) sample showing more voids and pores with relatively bigger agglomerated particles. The porosity is produced by the superheated gases escaping from the reaction. These porous powders are highly friable which facilitates easy grinding to obtain finer particle. This is believed to be related to the non-uniform distribution of temperature and mass flow in the combustion flame [16]. Fig. 2(c) shows TEM image of doped Nd_2O_3, reveals slight amount of agglomeration and porosity. The particles sizes appeared to be in the range of 30–130 nm and it is good agreement with SEM values.

3.3. UV–vis spectroscopy and band gap (E_g) measurements

The UV–vis absorption spectra of un-doped and Ni^{2+} doped Nd_2O_3 phosphor is shown in (Fig. S2). The spectra exhibit a broad and prominent absorption band with maximum at ~226–240 nm along with small absorption band at ~292 nm. The maximum absorption, which can arise due to transition between valence band to conduction band [17]. The weak absorption in the UV–vis region is expected to arise from transitions involving extrinsic states such as surface traps or defect states or impurities [18]. Smaller size particles are found to have high surface to volume ratio. This results in increase of defects distribution on the surface of nanomaterials. Thus the lower is the particle size, nanomaterials exhibit strong and broad absorption bands [19]. In Ni^{2+} doped Nd_2O_3 the particle size is in nanometer size which results high surface to volume ratio; as

a result, an increase of defects distribution on the surface of the nanomaterials.

The optical band gap energy (E_g) of un-doped and Ni^{2+} doped Nd_2O_3 phosphor was estimated by Tauc relation [20] and are shown in Fig. 3. The optical band gap associated with absorbance and photon energy by the following relation

$$(\alpha h\nu) \propto (h\nu - E_{gap})^k \tag{1}$$

where α – absorbance, h is the Planck's constant, ν is the frequency, E_{gap} is the optical band gap energy and k is a constant associated to the different types of electronic transitions (k = 1/2, 2, 3/2 or 3 for direct allowed, indirect allowed, direct forbidden and indirect forbidden transitions, respectively). According to the literature
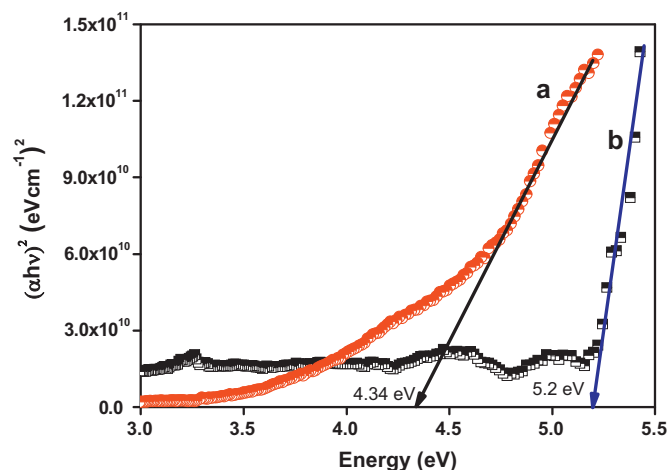

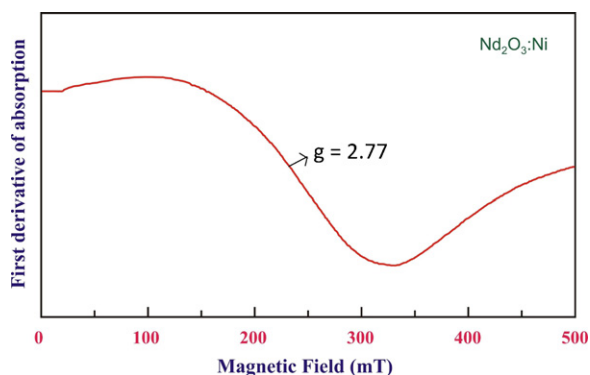**Fig. 3.** Direct band gap of (a) un-doped and (b) Ni^{2+} doped Nd_2O_3 nanophosphor.

Fig. 4. EPR spectrum of Nd_2O_3:Ni^{2+} (2 mol%) nanophosphor.

Fig. 5. Raman spectrum of Ni^{2+} doped Nd_2O_3 nanophosphor.

[21], the oxides are characterized by an indirect allowed electronic transition and hence, the $k = 2$ value was used as standard in Eq. (1). Thus, the E_{gap} values have been evaluated by extrapolating the linear portion of the curve or tail [$(\alpha h\nu)1/k = 0$] in the UV–vis absorption spectra.

It is observed from the figure the E_g value is less in un-doped sample when compared Ni^{2+} doped sample. The E_g value for Ni^{2+} doped Nd_2O_3 phosphor estimated from this relation is in good agreement with the literature [22]. The variation in band gap values in un-doped with doped samples can be related to the degree of structural order–disorder in the lattice which is able to change the intermediate energy level distribution within the band gap. This is attributed to particle size effect. The nanomaterials have large surface to volume ratio as a result, the formation of voids on the surface as well as inside the agglomerated particles. Such voids can cause fundamental absorption in the UV range [23].

In un-doped sample a high degree of structural defects may be present. When Ni^{2+} ions are doped into Nd_2O_3 matrix, it becomes more ordered structure with fewer defects. Consequently intermediate energy levels (deep and shallow holes) are minimized within the optical band gap and E_g increases. Further, the E_g values mainly depend on the preparation methods and different experimental conditions. In particular these key factors can favor or inhibit the formation of structural defects, which are able to control the degree of structural order–disorder of the material and consequently the number of intermediate energy levels within the band gap [22].

3.4. Electron paramagnetic resonance (EPR)

Fig. 4 shows the EPR spectrum of 2 mol% of Ni doped Nd_2O_3 phosphor at room temperature. The spectrum consists of a symmetric absorption at $g \approx 2.77$. As the Ni^{2+} ions belongs to d^8 configuration, the degenerate free ion 3F ground state of Ni^{2+} splits as a consequence of crystal field. In an octahedral environment the orbital singlet $^3A_{2g}$ has the lowest energy level. Using the spin-Hamiltonian [24]

$$\mathcal{H} = g\beta BS \tag{2}$$

with $S = 1$, an isotropic g factor is obtained which corresponds to the $|0\rangle - |\pm 1\rangle$ magnetic dipole transitions. Owing to the moderately high spin–orbit coupling, the isotropic g value for octahedrally co-ordinated Ni^{2+} ions departs from the free electron value ($g_e = 2.0023$).

The number of spins participating in resonance can be calculated by comparing the area under the absorption curve with that of a standard ($CuSO_4 \cdot 5H_2O$ in this study) of known concentration.
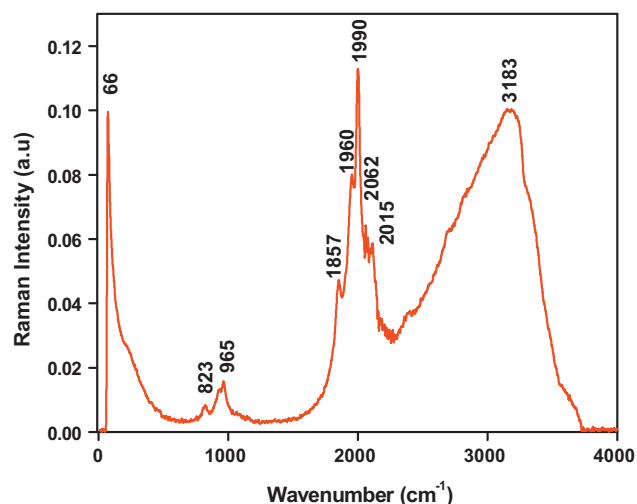
Weil et al. [25] gave the following expression which includes the experimental parameters of both sample and standard.

$$N = \frac{A_x(\text{Scan}_x)^2 G_{std}(B_m)_{std}(g_{std})^2[S(S+1)]_{std}(P_{std})^{1/2}}{A_{std}(\text{Scan}_{std})^2 G_x(B_m)_x(g_x)^2[s(s+1)]_x(P_x)^{1/2}}[\text{std}] \tag{3}$$

where A is the area under the absorption curve which can be obtained by double integrating the first derivative EPR absorption curve, scan is the magnetic field corresponding to unit length of the chart, G is the gain, B_m is the modulation field width, g is the g factor, S is the spin of the system in its ground state. P is the power of the microwave source. The subscripts 'x' and 'std' represent the corresponding quantities for Nd_2O_3:Ni^{2+} and the reference ($CuSO_4 \cdot 5H_2O$) respectively. The number of Ni^{2+} ions participating in resonance at room temperature for 2 mol% Ni^{2+} ions in Nd_2O_3 phosphor is found to be 5.596×10^{23}.

The EPR data can be used to calculate the paramagnetic susceptibility (χ) of the sample using the formula [26]

$$\chi = \frac{Ng^2\beta^2 J(J+1)}{3k_BT} \tag{4}$$

where 'N' is the number of spins per m^3, 'β' is the Bohr magneton, 'J' is the total angular momentum, 'k_B' is the Boltzmann constant and 'T' is the absolute temperature. N can be taken from Eq. (3). The paramagnetic susceptibility (χ) thus evaluated is found to be 30.67×10^{-3} m^3 kg^{-1}.

3.5. Raman spectroscopy

Raman spectroscopy is a powerful tool for characterizing the nanomaterials; it is an in situ and non-destructive method. Fig. 5 shows the Raman spectrum of combustion synthesized Ni^{2+} (2 mol%) doped Nd_2O_3 phosphor recorded with an excitation wavelength of 633 nm laser beam. A well-defined Raman peaks at ~823, 965, 1857, 1960, 1990, 2062, and broad peak at 3183 cm^{-1} were observed. The major peaks observed are assigned to be F_g and combination of $A_g + E_g$ modes [27]. According to factor group theory 22 active Raman modes ($4A_g$, $4E_g$ and $14F_g$) have been predicted for the Nd_2O_3 A-type and C type bixbyite structured rare earth sesquioxides. In our earlier studies [28], combustion and hydrothermally synthesized Nd_2O_3 nano phosphor show Raman modes at ~1827, 1940, 1996, 2053 and 2110 cm^{-1}. The observed active Raman modes in the present studies are fewer in number when compared to Nd_2O_3 synthesized by hydrothermal method [28]. This might
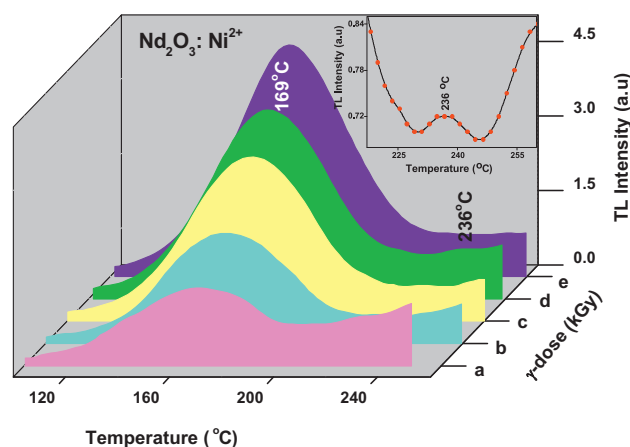
Fig. 6. TL glow curves of $Nd_2O_3:Ni^{2+}$ γ-irradiated for (a) 0.228 kGy (b) 0.685 kGy (c) 1.142 kGy (d) 1.6 kGy (e) 2.057 kGy (inset: enlarged view of TL glow peak from 220 to 260 °C).

be due to type of synthesis method, particle size effect, precursors used during synthesis, etc.

Further, they observed frequency shift and broadening of Raman peaks in their studies which might be attributed to nano sized particles. Urben and Cornilsen [29] reported Raman frequency undergoes a red shift with a decrease in the radius of nano solid. Pan et al. [17] suggest that this red shift arises from the cohesive bond weakening of the lower coordinated atoms near the surface region of the nano grain. Further this shift may also be due to the short-range interactions between a phonon and photon, and when the size is decreased the momentum conservation will be relaxed and the Raman active modes will not be limited at the center of the Brillounin zone as a result there is a decrease in Raman wave number. Dilawar et al. [27] recorded Raman Spectra for the rare earth sesquioxides namely Y_2O_3, Sm_2O_3, Eu_2O_3, Gd_2O_3, Dy_2O_3, Ho_2O_3, Er_2O_3 and Yb_2O_3 under ambient conditions. Strongest Raman peaks are observed at 379, 344, 338, 363, 372, 374, 373 and 365 cm^{-1} respectively in all the compounds which are assigned as F_g mode and $A_g + E_g$ modes.

3.6. Thermoluminescence (TL) studies

TL is a powerful technique used for estimation of doses of high-energy ionizing radiations as the energy absorbed during irradiation and the TL intensity on stimulation (heating) is proportional to the radiation flux (doses). Recent studies on different luminescent nano materials have showed that they have a potential application in dosimetry of ionizing radiations for the measurements of high doses using the TL technique, where the conventional microcrystalline phosphors saturate [17,30–32]. This saturation occurs due to the ionized zones overlapping each other in the micro material at higher doses. However, with the use of very tiny particles such as nanoscale TLD materials, this problem can overcome to a major extent. The TL results of the reported nano materials have revealed very imperative characteristics such as simple glow peak structure, linear increase in intensity with dose, simple trap distribution. This has encouraged us to study the TL of $Nd_2O_3:Ni^{2+}$ nanophosphor using gamma irradiation in the dose range 0.28–2.057 kGy.

$Nd_2O_3:Ni^{2+}$ system as a dosimeter is a new concept. Fig. 6 shows the TL glow curves of γ-irradiated $Nd_2O_3:Ni^{2+}$ nanophosphor. The nanocrystalline phosphor is warmed at a heating rate of 5 °C s^{-1}. A well resolved glow peak at 169 °C along with a shouldered peaks appears at around 236 °C. The variation of TL glow peak intensity with accumulated dose was studied and is shown in (Fig S3). It

is observed that, the TL intensity increases with increasing dose. This linear behavior of the sample is useful for dosimetric application. Further, it is noticed that there is no appreciable shift in the glow peak positions with increase of gamma dose. The appearance of two peaks in the glow curve indicates that there are possibly two kinds of trapping sites generated due to gamma irradiation. The shallow trapping center leads to the resolved peak at lower temperature and the other deeper center gives rise to shouldered peak at higher temperature. The intensity of the higher temperature glow peak increases linearly with dose. This might be due to the high surface to volume ratio, which results in a higher surface barrier energy for the nanoparticles. On increasing the dose, the energy density crosses the barrier and a large number of defects are produced in the nanoparticles which ultimately keep on increasing with the dose till saturation is achieved [33]. In our earlier work TL studies of $Nd_2O_3:Eu^{3+}$ show a well resolved glow peak at 426 K. It was observed that intensity of this glow peak increases linearly with γ-dose (100–400 Gy). Further, simple glow peak structure, less fading, sensitivity retains after several cycles of exposure and readouts, excellent reusability show $Nd_2O_3:Eu^{3+}$ has a potential use in radiation dosimetry [34].

It is observed that from the figure for lower dose samples, the traps/defects generated appear to be very less due to surface barrier. Hence the glow curve has minimum intensity and the peak appears at lower temperature. As the temperature increases, the surface barrier energy also increases, and the lower dose (0.228 kGy) is not sufficient to create the defects. The increase in TL intensity with dose can be explained on the basis of track interaction model [35,36]. According to this model, the number of traps generated by the high energy radiation in a track depends upon the cross section and the length of the track inside the matrix. In the case of nanomaterials, the length of the track generated by high energy radiation is of few tenths of nanometers. At low doses, there exist a few trap centers or luminescent centers owing to the small size of the particles. As the dose increases, the TL intensity increases as the cross section would increase with increase in dose.

TL characteristic of the phosphor requires the knowledge of trapping parameters such as activation energy (E) of the traps involved in TL emission and the order of kinetics (b) associated with the glow peaks. Here, E is a measure of the energy required to eject an electron from the defect center to the conduction band. The order of kinetics b is a measure of the probability that a free electron gets retrapped. This retrapping effect increases with density of empty traps. It is known that, equal concentrations of trapped electrons (n) and recombination centers (r) lead to give a condition for the first order kinetics. For second order kinetics, recombination and retrapping probabilities are found to be equal along with the condition $r < n$ [35]. The trapping parameters ware calculated using Chen's set of empirical equations [37] for the peak shape method as summarized below. A typical result for a glow curve of γ-irradiated for 0.685 kGy is shown in Fig. 7. The TL glow curve was first deconvoluted based on Gaussian function (Fig. 7) and then analyzed the individual deconvoluted peak using Chen's peak shape method [30].

The activation energy (E) and the order of kinetics are estimated using the following relations (symbols have standard meaning)

$$E_\alpha = c_\alpha \left(\frac{kT_m^2}{\alpha} \right) - b_\alpha (2kT_m) \tag{5}$$

where $\alpha = \tau$, δ and ω with $\tau = T_m - T_1$, $\delta = T_2 - T_m$ and $\omega = T_2 - T_1$

$$C_\tau = 1.51 + 3.0(\mu_g - 0.42), \quad b_\tau = 1.58 + 4.2(\mu_g - 0.42) \tag{6}$$

$$C_\delta = 0.976 + 7.3(\mu_g - 0.42), \quad b_\delta = 0 \tag{7}$$

$$C_\omega = 2.52 + 10.2(\mu_g - 0.42), \quad b_\omega = 1 \tag{8}$$

Table 2
Kinetic parameters estimated using Chen's glow peak shape method in Nd_2O_3:Ni^{2+} (2 mol%) nanophosphor irradiated with different γ-dose.

| γ-Dose (kGy)	Peak	T_m (°C)	Order of kinetics b (μ_g)	Activation energy (eV)				Frequency factor (s^{-1})
				E_τ	E_δ	E_ω	E_{ave}	
2.057	1	134	(2)0.49	1.124	1.137	1.138	1.133	2.4E+15
	2	161	(2)0.49	1.123	1.138	1.137	1.133	2.8E+14
	3	172	(2)0.49	1.390	1.383	1.395	1.389	1.3E+17
	4	194	(2)0.49	1.630	1.606	1.629	1.622	7.9E+18
1.600	1	138	(2)0.51	1.096	1.086	1.096	1.093	5.3E+14
	2	161	(2)0.51	1.464	1.414	1.446	1.441	1.4E+18
	3	184	(2)0.49	1.359	1.365	1.371	1.365	2.4E+16
	4	216	(2)0.52	1.992	1.799	1.893	1.895	9.1E+20
1.142	1	135	(2)0.52	0.895	0.902	0.902	0.900	2.2E+12
	2	159	(2)0.50	1.336	1.318	1.335	1.329	7.6E+16
	3	184	(2)0.49	1.558	1.538	1.559	1.551	3.2E+18
	4	223	(2)0.48	0.659	0.739	0.700	0.699	1.1E+08
0.685	1	148	(2)0.48	0.808	0.854	0.835	0.833	1.4E+11
	2	155	(2)0.48	1.403	1.325	1.338	1.356	2.2E+17
	3	176	(2)0.51	1.322	1.142	1.161	1.208	7.1E+14
	4	209	(2)0.49	0.753	0.567	0.539	0.62	2.4E+07
0.228	1	138	(2)0.49	0.829	0.582	0.568	0.66	1.5E+09
	2	161	(2)0.51	1.464	1.041	1.073	1.193	1.5E+15
	3	176	(2)0.49	1.003	0.569	0.559	0.71	1.0E+09
	4	208	(2)0.51	0.791	0.594	0.572	0.652	5.7E+07
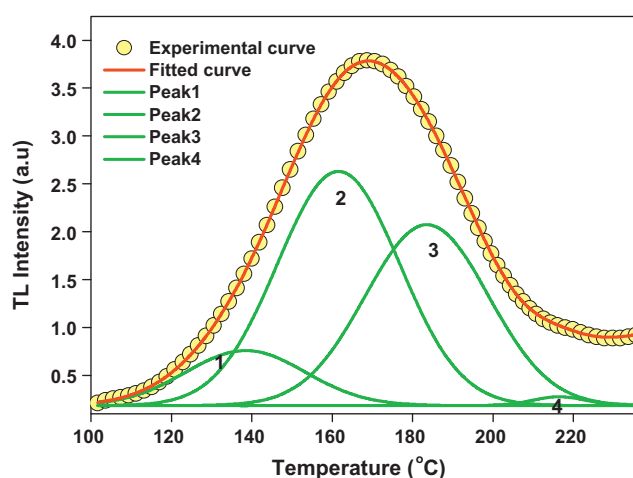
Fig. 7. Glow curve deconvolution of Ni^{2+} doped irradiated with 1.6 kGy gamma dose at a heating rate of 5 °C s^{-1}.

The form factor (symmetry factor) is given by

$$\mu_g = \frac{T_2 - T_m}{T_2 - T_1} \tag{9}$$

The nature of the kinetics can be found by the form factor. Theoretically, the value of geometrical form factor (μ_g) is close to 0.42 for first order kinetics and 0.52 for second order kinetics. In the present study, the value of μ_g is very close to 0.52 and it falls under second order kinetics. The trapping parameters of Nd_2O_3:Ni^{2+} obtained using peak shape method irradiated with different gamma dose is given in Table 2.

4. Conclusions

Ni^{2+} (2 mol%) doped Nd_2O_3 nanophosphor has been successfully synthesized by a low temperature solution combustion method using ODH as fuel. PXRD results confirm that the nanophosphor attain hexagonal structure without any secondary phase. The particle size of un-doped and Ni doped product Nd_2O_3 has been calculated by Williamson–Hall (W–H) plots and Scherrer's formula

is found to be in the range of ∼21–33 nm. TEM image confirms the nano size crystalline nature of Ni doped Nd_2O_3. SEM micrographs of un-doped and Ni doped Nd_2O_3 show highly porous, agglomeration with large voids. The EPR spectrum suggests that the site symmetry around Ni^{2+} ions is predominantly octahedral. From UV–vis studies, the maximum absorption at 226–240 nm can arise due to transition between valence band to conduction band. The weak absorption in the UV–vis region is expected to arise from transitions involving extrinsic states such as surface traps or defect states or impurities. Raman study show major peaks, which are assigned, to F_g and combination of $A_g + E_g$ modes. TL properties of Ni^{2+} doped Nd_2O_3 nanophosphors were investigated after irradiation with gamma rays in the dose range 0.228–2.57 kGy at room temperature (RT). Two TL glow peaks were recorded at 169 and 236 °C at a warming rate of 5 °C s^{-1}. It is observed that the glow peak intensity at 169 °C increases linearly with gamma dose which suggest that Nd_2O_3:Ni^{2+} is suitable for radiation dosimetry applications.

Appendix A. Supplementary data

Supplementary data associated with this article can be found, in the online version, at doi:10.1016/j.saa.2012.02.082.

References

[1] X. Qu, J. Dai, J. Tian, X. Huang, Z. Liu, Z. Shen, P. Wang, J. Alloys Compd. 469 (2009) 332–335.
[2] L. Qian, Y. Gui, S. Guo, Q. Gong, X. Qian, J. Phys. Chem. Solids 70 (2009) 688–693.
[3] R. Bazzi, M.A. Flores-Gonzalez, C. Louis, K. Lebbou, C. Dujardin, A. Brenier, W. Zhang, O. Tillement, E. Bernstein, J. Lumin. 445 (2003) 102–103.
[4] A.G. Dedov, A.S. Loktev, I.I. Moiseev, A. Aboukais, J.F. Lamonier, I.N. Filimonov, Appl. Catal. A 245 (2003) 209–220.
[5] S. Pengpanich, V. Mecyoo, T. Rirksomboon, J. Chem. Eng. Jpn. 38 (2005) 49–53.
[6] B. Zhaorigetu, G. Ridi, L. Min, J. Alloys Compd. 427 (2007) 235–237.
[7] M. Zawadzki, L. Kepinski, J. Alloys Compd. 380 (2004) 255–259.

[8] K.C. Patil, M.S. Hegde, T. Rattan, S.T. Aruna, Chemistry of Nanocrystalline Oxide Materials: Combustion Synthesis, Properties and Applications, World Scientific Publication Co. Pvt. Ltd., UK, 2008.

[9] S. Ekambaram, N. Arul Dhas, K.C. Patil, Int. J. Self Propag. High Temp. Synth. 4 (1995) 85–93.

[10] R. Bazzi, A. Brenier, P. Perriat, O. Tillement, J. Lumin. 113 (2005) 161–167.

[11] W. Yang, Y. Qi, Y. Ma, X. Li, X. Guo, J. Gao, M. Chen, Mater. Chem. Phys. 84 (2004) 52–57.

[12] B.M. Nagabhushana, Ph.D. Thesis, Bangalore University, 2008.

[13] P. Klug, L.E. Alexander, X-ray Diffraction Procedure, Wiley, NewYork, 1954.

[14] A. Jagannatha Reddy, M.K. Kokila, H. Nagabhushana, J.L. Rao, B.M. Nagabhushana, C. Shivakumara, R.P.S. Chakradhar, Spectrochim. Acta A 79 (2011) 476–480.

[15] G.K. Willamson, W.H. Hall, Acta Metall. 1 (1953) 22–31.

[16] B. Nagappa, G.T. Chandrappa, Microporous Mesoporous Mater. 106 (2007) 212–218.

[17] L.K. Pan, Q. Sunchang, C.M. Li, J. Phys. Chem. B 108 (2004) 3404–3406.

[18] H.Q. Cao, X.Q. Qiu, B. Luo, Y. Liang, Y.H. Zhang, R.Q. Tan, M.J. Zhao, Q.M. Zhu, Adv. Funct. Mater. 14 (2004) 243–246.

[19] A. Emeline, G.V. Kataeva, A.S. Litke, A.V. Rudakova, V.K. Ryabchuk, N. Serpone, Langmuir 14 (1998) 501–5022.

[20] J. Tauc, In: F. Abeles (Ed.), Optical Properties of Solids, North Holland publishers, Amsterdam, 1970.

[21] N. Dhananjaya, H. Nagabhushana, B.M. Nagabhushana, B. Rudraswamy, C. Shivakumara, R.P.S. Chakradhar, J. Alloys Compd. 509 (2011) 2368–2374.

[22] X. Lu, X. Li, F. Chen, C. Ni, Z. Chen, J. Alloys Compd. 476 (2009) 958–962.

[23] N. Salah, S.S. Habib, Z.H. Khan, S.A. Hamedi, S.P. Lochab, J. Lumin. 129 (2009) 192–196.

[24] A. Abragam, B. Bleaney, Electron Paramagnetic Resonance of Transition Ions, Clarendon Press, Oxford, 1970, p. 175.

[25] J.A. Weil, J.R. Bolton, J.E. Wertz, Electron Paramagnetic Resonance Elementary Theory and Practical Applications, John Wiley, New York, 1994, p. 498.

[26] N.W. Aschcroft, N.D. Mermin, Solid State Physics, Harcourt College Publishers, 2001, p. 656.

[27] N. Dilawar, S. Mahrotra, D. Varandani, B.V. Kumaraswamy, S.K. Halder, A.K. Bandyopadhyay, Mater. Charact. 59 (2008) 462–467.

[28] B. Umesh, B. Eraiah, H. Nagabhushana, B.M. Nagabhushana, G. Nagaraja, C. Shivakumara, R.P.S. Chakradhar, J. Alloys Compd. 28 (2011) 1146–1151.

[29] W. Urben Marek, C. Cornilsen Bahn, J. Phys. Chem. Solids 48 (1984) 475–480.

[30] R. Chen, S.W.S. Mckeever, Theory of Thermoluminescence and Related Phenomena, World Scientific Press, Singapore, 1997.

[31] J.R. Cameron, N. Suntharalingam, G.N. Kenney, Thermoluminescent Dosimetry, The University of Wisconsin Press, Madison, 1968.

[32] A. Pandey, S. Bahl, K. Sharma, R. Ranjan, P. Kumar, S.P. Lochab, V.E. Aleynikov, Nucl. Instrum. Methods Phys. Res. B 269 (2011) 216–222.

[33] S.P. Lochab, P.D. Sahare, R.S. Chauhan, N. Salah, A. Pandey, J. Phys. D: Appl. Phys. 39 (2006) 1786–1792.

[34] B. Umesh, B. Eraiah, B.M. Nagabhushana, H. Nagabhushana, H.B. Premkumar, C. Shivakumara, C. Hanumantharayappa, R.P.S. Chakradhar, Philos. Mag. Lett. 89 (2009) 589–597.

[35] Y.S. Horowitz, M. Rosenkrantz, S. Mahajna, D. Yossian, J. Phys. D: Appl. Phys. 29 (1996) 205–217.

[36] Y.S. Horowitz, O. Avila, M. Rodrigues-Villafuerte, Nucl. Instrum. Methods Phys. Res. B 184 (2001) 85–112.

[37] R. Chen, Y. Kirsh, Analysis of Thermally Stimulated Processes, Pergamon, New York, 1981.